MATERIALS SCIENCE

Large enhancement of ferroelectric properties of perovskite oxides via nitrogen incorporation

Tao Wang[1]†, Fenghui Gong[2]†, Xue Ma[3]†, Shen Pan[1]†, Xian-Kui Wei[4]†, Changyang Kuo[5,6], Suguru Yoshida[7], Yu-Chieh Ku[5], Shuai Wang[1], Zhenni Yang[4], Sankalpa Hazra[7], Kelvin H. L. Zhang[4], Xingjun Liu[1], Yunlong Tang[2], Yin-Lian Zhu[2], Chun-Fu Chang[8], Sujit Das[9], Xiuliang Ma[2], Lang Chen[10], Bin Xu[3], Venkatraman Gopalan[7], Laurent Bellaiche[11,12], Lane W. Martin[13,14], Zuhuang Chen[1]*

Perovskite oxides have a wide variety of physical properties that make them promising candidates for versatile technological applications including nonvolatile memory and logic devices. Chemical tuning of those properties has been achieved, to the greatest extent, by cation-site substitution, while anion substitution is much less explored due to the difficulty in synthesizing high-quality, mixed-anion compounds. Here, nitrogen-incorporated $BaTiO_3$ thin films have been synthesized by reactive pulsed-laser deposition in a nitrogen growth atmosphere. The enhanced hybridization between titanium and nitrogen induces a large ferroelectric polarization of 70 μC/cm^2 and high Curie temperature of ~1213 K, which are ~2.8 times larger and ~810 K higher than in bulk $BaTiO_3$, respectively. These results suggest great potential for anion-substituted perovskite oxides in producing emergent functionalities and device applications.

INTRODUCTION

Perovskite oxides with the general formula ABO_3 constitute a rich material playground for emergent physical properties and novel devices concepts. In the past few decades, substantial progress has been made in both *A*- and/or *B*-site cation doping, with giant piezoelectricity in (1-*x*)$Pb(Mg_{1/3}Nb_{2/3})O_3$-(*x*)$PbTiO_3$ (*1*), high dielectric tunability in $Ba_{1-x}Sr_xTiO_3$ (*2*), colossal magnetoresistance in $La_{1-x}Ca_xMnO_3$ (*3*), etc. Recently, mixed-anion perovskites have garnered increasing attention due to their unique phenomena that are unattainable in simple oxides, including fast anionic conduction (*4*), visible-light photocatalysis (*5*), strain-tunable anion arrangements (i.e., cis and trans configurations) (*6*–*8*), and enhanced ferroelectricity (*8*, *9*). However, compared to cation substitution, anion (oxygen-site) substitution is much less explored due to the high stability of the metal-oxygen bond, which makes it challenging to synthesize mixed-anion perovskites (*10*, *11*). Thus, the field of anion-substituted perovskite oxides remains relatively underexplored and thus may hide the potential impact of this approach to engineer functionalities of perovskite materials (*11*–*13*). As compared with other anions, nitrogen has multiple similarities in electronic and structural characteristics to those of oxygen, such as the ionic radius (1.46 Å for N^{-3}, and 1.40 Å for O^{-2}) (*14*). Hence, nitrogen substitution may retain the perovskite structure if the overall electroneutrality condition is met. Nevertheless, unlike cation-substituted perovskite oxides, synthesis of nitrogen-substituted perovskite oxides by conventional direct, solid-state reaction processes in an inert nitrogen atmosphere is challenging, as the direct reaction between N_2 and oxides requires a very high activation energy due to the strong triple bond of N_2 (*15*). Thus, such mixed-anion perovskites are typically synthesized either by high-temperature ammonolysis reaction under NH_3 flow (*16*) or by a two-step process via a combination of topochemical reduction of perovskite oxides and further low-temperature ammonolysis reaction (*17*). These synthetic approaches, however, have serious disadvantages for ferroelectrics. For example, the transition metal cations (e.g., Ti^{4+}) are easily reduced by the reducing reagents (e.g., CaH_2 and NH_3), which is deleterious for the electrical resistivity of the material (*18*). Moreover, these methods might also introduce hydrogen into the materials, which can degrade ferroelectric properties (*19*). Therefore, if nitrogen-substituted perovskite oxides can be readily synthesized, there is potential to open up numerous advances in this class of materials.

RESULTS

Films growth

One deposition technique could be useful in this regard. Pulsed-laser deposition (PLD) is a highly nonequilibrium growth technique and thus could allow for the growth of high-quality anion-substituted perovskite thin films. The highly energetic species in the ablation plasma can react with gas molecules to produce compounds that incorporate all species in the system (*10*, *20*). Therefore, even nitrogen gas (i.e., N_2) could be used as the reaction gas to synthesize nitrogen-substituted perovskite oxide thin films by PLD. Previous studies have successfully used PLD to fabricate oxynitride epitaxial thin films, including nitrogen-substituted perovskite $SrTiO_3$ thin films (*21*–*23*)

[1]State Key Laboratory of Advanced Welding and Joining of Materials and Structures, School of Materials Science and Engineering, Harbin Institute of Technology, Shenzhen 518055, China. [2]Shenyang National Laboratory for Materials Science, Institute of Metal Research, Chinese Academy of Sciences, Shenyang 110016, China. [3]Jiangsu Key Laboratory of Frontier Material Physics and Devices, School of Physical Science and Technology, Soochow University, Suzhou 215006, China. [4]College of Chemistry and Chemical Engineering, Xiamen University, Xiamen 361005, China. [5]Department of Electrophysics, National Yang Ming Chiao Tung University, Hsinchu 30010, Taiwan. [6]National Synchrotron Radiation Research Center, 101 Hsin-Ann Road, Hsinchu 30076, Taiwan. [7]Materials Research Institute and Department of Material Science & Engineering, Pennsylvania State University, University Park, PA 16802, USA. [8]Max-Planck Institute for Chemical Physics of Solids, Nöthnitzer Str. 40, 01187 Dresden, Germany. [9]Materials Research Centre, Indian Institute of Science, Bangalore 560012, India. [10]Department of Physics, Southern University of Science and Technology, Shenzhen 518055, China. [11]Physics Department and Institute for Nanoscience and Engineering, University of Arkansas, Fayetteville, AR 72701, USA. [12]Department of Materials Science and Engineering, Tel Aviv University, Ramat Aviv, Tel Aviv 6997801, Israel. [13]Department of Materials Science and Engineering, University of California, Berkeley, CA 94720, USA. [14]Materials Sciences Division, Lawrence Berkeley National Laboratory, Berkeley, CA 94720, USA.
*Corresponding author. Email: zuhuang@hit.edu.cn
†These authors contributed equally to this work.

and $SrTaO_2N$ epitaxial thin films (*8*). However, to the best of our knowledge, direct observations of enhanced polarization in oxynitride thin films have not been reported to date. Here, we present the successful fabrication of nitrogen-incorporated $BaTiO_3$ thin films exhibiting enhanced ferroelectricity on $SrTiO_3$ (001) substrates using PLD in a nitrogen/oxygen gas mixture. The dynamic gas pressure during film growth was kept at 20 mtorr and the ratio of nitrogen/oxygen was controlled by a flowmeter (Fig. 1A).

Structural characterization

All thin films have smooth surface with a terraced feature, where the root mean square roughness is <500 pm (Fig. 1A). X-ray diffraction studies reveal that all the films grown in different atmospheres are single-phase, 00*l*-oriented (Fig. 1B and fig. S1). The smooth interface of the thin films was evidenced by the Laue fringes near diffraction peaks (Fig. 1B). It is worth noting that $BaTiO_3$ films grown in a nitrogen atmosphere exhibit less clear thickness oscillation compare to those in a pure oxygen atmosphere. This difference is likely related to the incorporation of nitrogen into the film, as confirmed by subsequent microstructural analysis of films grown in a 100% N_2 atmosphere. X-ray rocking curve studies further demonstrate that the nitrogen growth atmosphere does not cause the deterioration of the crystalline quality of the films (fig. S2). Upon increasing the nitrogen concentration ratio in the nitrogen/oxygen gas mixture, it is interesting to note that the out-of-plane lattice parameter markedly increases from ~4.06 to ~4.33 Å; that is, the *c*/*a* ratio of the film increases to ~1.11 or 9.7% larger than that of bulk $BaTiO_3$ (Fig. 1C). Subsequent off-axis reciprocal space mapping (RSM) about the 103-diffraction condition reveals that the films grown in 50 and 100% N_2 atmospheres are coherently strained to the underlying substrate (Fig. 1D and fig. S3).

To confirm whether the increase of the out-of-plane lattice parameter originates from isolated oxygen vacancies or not, we annealed the films grown in 100% N_2 atmosphere in an oxygen atmosphere at 550°C (fig. S4). The film still exhibits notable out-of-plane lattice expansion after annealing. In another control experiment, we grew $BaTiO_3$ films in different argon/oxygen gas mixtures, but we did not observe similar notable expansion in the out-of-plane lattice parameter (fig. S5). Therefore, it is less likely that isolated oxygen vacancies are the primary cause of the observed notable lattice expansion. Out-of-plane lattice parameter of $BaTiO_3$ thin films can increase with laser fluence (which correlations to the adatom kinetic energy) (*24*). Therefore, we also compare $BaTiO_3$ thin films grown in 100% N_2 under different laser fluences (fig. S6). We observed no change in the out-of-plane lattice parameters of the films. Therefore, the large out-of-plane lattice parameter in $BaTiO_3$

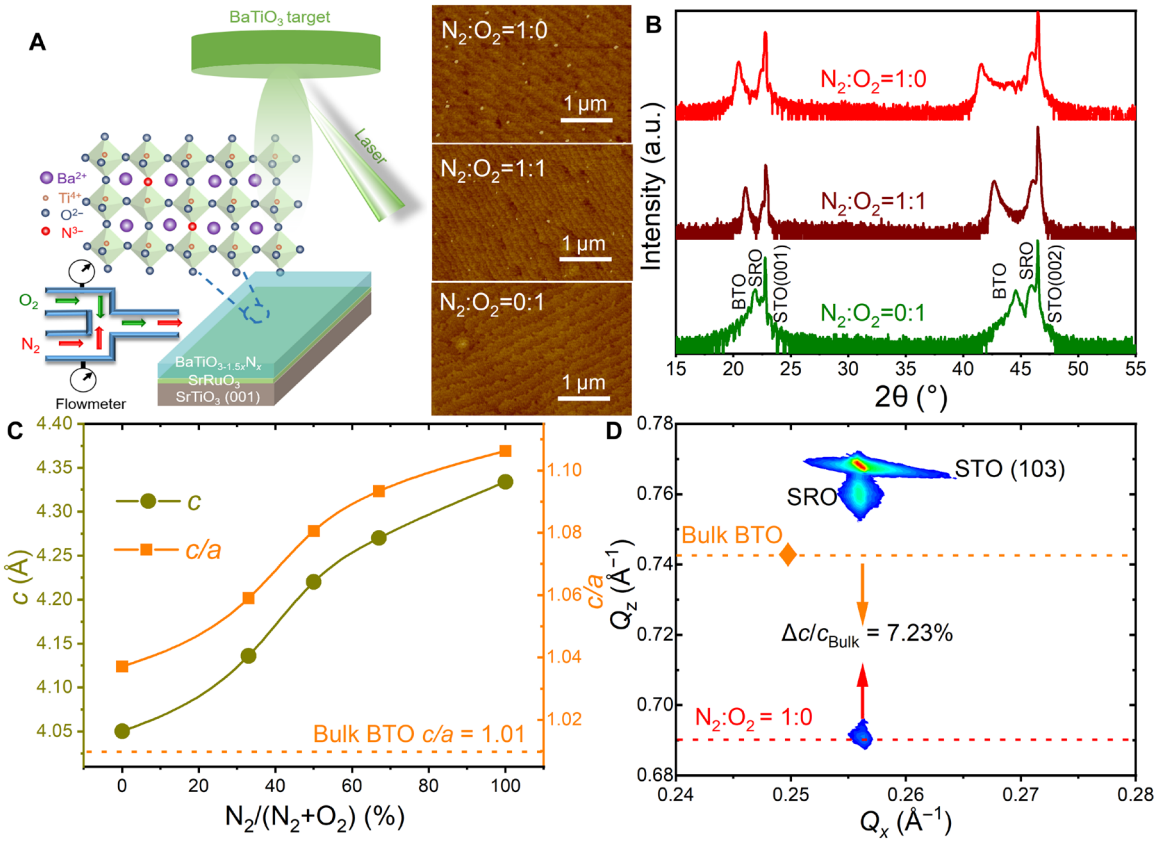

Fig. 1. Enhanced tetragonality in $BaTiO_3$ thin films by reactive pulsed-laser deposited technique in N_2-containing growth atmosphere. (**A**) The schematic diagram of the thin films grown in mixed atmosphere with N_2 and O_2. (**B**) θ-2θ x-ray diffraction scans of the films grown in different atmospheres. (**C**) The out-of-plane lattice constant and *c*/*a* of the films grown in different nitrogen content. (**D**) The RSM result of the film grown in 100% nitrogen content around the $SrTiO_3$ (103) diffraction spots. To illustrate the change of lattice parameter of the thin film relative to that of bulk $BaTiO_3$, $\Delta c/c_{Bulk}$ is used, where Δc corresponds to the difference between *c* lattice parameter of the film and that of bulk $BaTiO_3$.

film grown in 100% N_2 may not be caused by laser fluence–induced knock-on defects, but, instead, it appears to be possibly related to anion substitution from growth in the nitrogen atmosphere.

We used high-resolution scanning transmission electron microscopy (STEM) imaging to obtain other structural information. We show a representative cross-sectional image of the 30-nm-thick film grown on a $SrRuO_3$-buffered $SrTiO_3$ substrate that has a sharp interface between the $SrRuO_3$ and $BaTiO_3$, which is indicative of the high quality of the film along the growth direction (figs. S7 and S8). We found, regardless of the nitrogen/oxygen gas mixture, that the in-plane lattice parameters of all films are nearly uniform, while the out-of-plane *c* lattice parameters of the films grown in nitrogen-containing atmospheres become much larger than that of the film grown in pure oxygen atmosphere. To illustrate the differences between the films grown in different atmospheres, we extracted the local *c*/*a* lattice parameter ratio from the high-angle annular dark-field images (fig. S8C). Remarkably, while the average *c*/*a* ratio from x-ray is ~1.11 (Fig. 1C), it can vary throughout the film and, locally, can be as large as ~1.27 for film grown in 100% nitrogen (fig. S8C). In contrast, we observed a *c*/*a* ratio of ~1.04 for film grown in 100% oxygen both macroscopically via x-ray studies (Fig. 1C) and locally via the STEM imaging (fig. S7). Electron energy loss spectroscopy (EELS) measurements reveal that nitrogen is doped into the film grown in 100% nitrogen atmosphere (figs. S9 and S10). Furthermore, integrated differential phase contrast (iDPC) STEM is performed to evaluate polarization displacement (*25*), specifically the displacement of Ti atoms (ΔZ_{Ti}) relative to the center of its four neighboring anions. The position of Ba atoms, Ti atoms, and anions can be clearly discerned from iDPC images based on atom column intensity (Fig. 2, A and B, and fig. S11 to S13). Using iDPC images, we calculated the ΔZ_{Ti} values of the films grown in different atmospheres. The ΔZ_{Ti} is observed to increase from ~0.2 to ~0.4 Å as the nitrogen content in gas mixture increases from 0 to 100%.

Our observations suggest that nitrogen incorporation leads to rather dramatic structural changes in the films. To confirm that nitrogen incorporation is truly being achieved, we probed the chemical composition of the films via x-ray photoelectron spectroscopy (XPS). Spectra taken about the location of the nitrogen 1*s* peak (Fig. 2C) for the films grown in different atmospheres reveal no signal of nitrogen in the films grown in 100% oxygen (bottom, Fig. 2C). As the nitrogen content in the gas mixture increases to 50%, we observed a clear nitrogen 1*s* peak (middle, Fig. 2C), which we can decompose into a main peak at ~399.6 eV (which we assigned to molecularly chemisorbed nitrogen or NO_x in interstitial positions) and a secondary peak at ~397.4 eV (which corresponds to Ti-N bonding due to the substitutional nitrogen at the oxygen site) (*26*, *27*). Upon further increasing the nitrogen in the gas mixture to 100%, the nitrogen 1*s* peak at ~397.4 eV increases (top, Fig. 2C), indicating that more nitrogen is substituted into the oxygen. Using the sensitivity factor method (*28*), the concentration of substituted

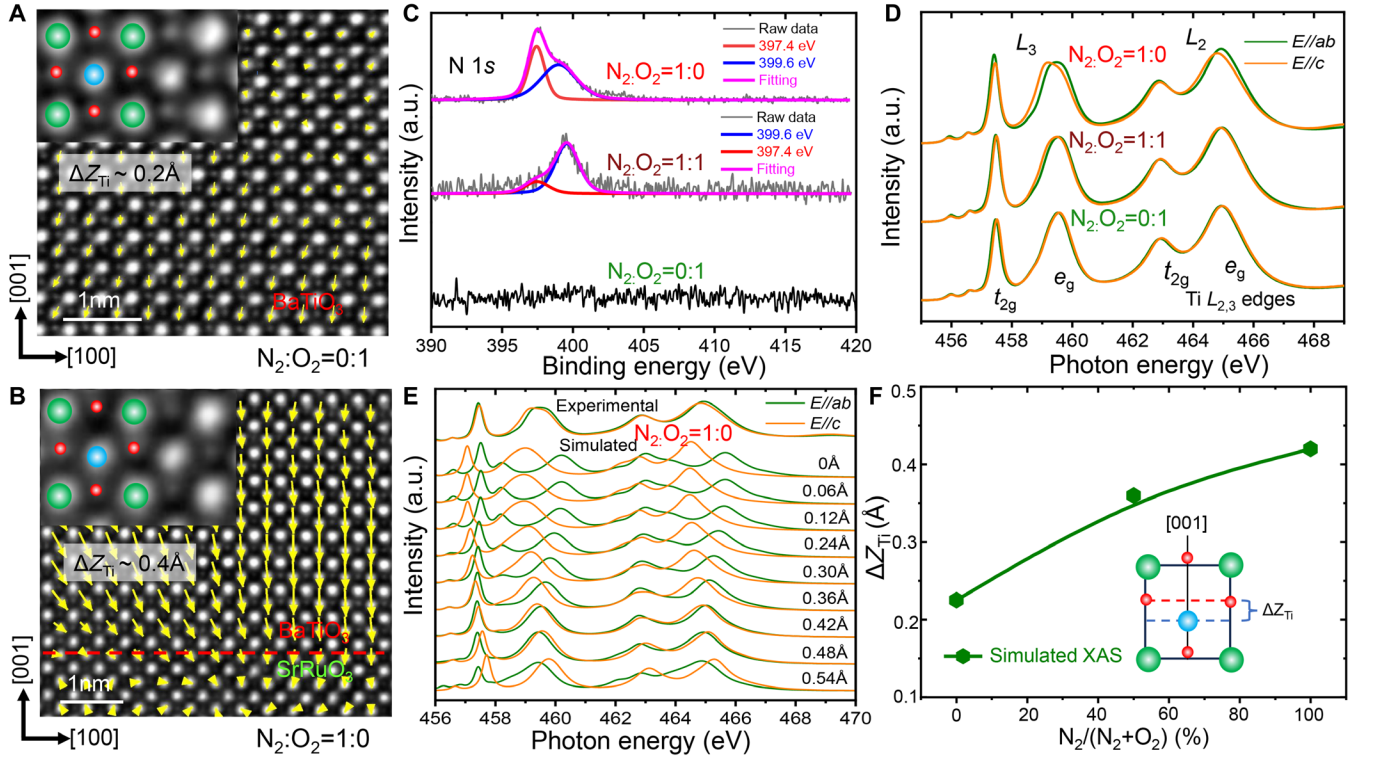

Fig. 2. The microstructures of $BaTiO_3$ thin films grown in different atmospheres. (**A** and **B**) Superposition of the ΔZ_{Ti} displacement vectors with the experimental iDPC images of the films grown in different atmospheres. The insets show partially enlarged iDPC images and yellow arrows represent ΔZ_{Ti} vectors. The green, blue, and red balls represent Ba, Ti, and anions, respectively. (**C**) Experimental and simulated XPS spectra for N 1*s*; (**D**) Polarized XAS spectra for Ti $L_{2,3}$ edges. (**E**) Simulated Ti $L_{2,3}$ edges XAS spectra for the film grown in 100% N_2. (**F**) The variation of ΔZ_{Ti} values obtained from simulated XAS spectra with N_2 content in gas mixture. The inset shows sketch diagram of ΔZ_{Ti}.

nitrogen we calculated at the oxygen site is ~7 atomic % (at %) for the film grown in 100% nitrogen. Furthermore, the substitution of nitrogen for oxygen can be expressed by the defect equation: $N_2 \xrightarrow{BaTiO_3} 2N'_O + V^{\bullet\bullet}_O$, where the charge neutrality is achieved via coformation of oxygen vacancies with N'_O defects. To confirm this coformation, we measured the oxygen 1*s* XPS spectra of the films grown in different nitrogen/oxygen gas mixtures (fig. S14). After fitting, we found that concentration of oxygen vacancies increases with increasing nitrogen content in the gas mixture, confirming the defect equation (and assuring charge compensation) and coformation of oxygen vacancies.

To reveal the microscopic origin of the increased lattice expansion in the nitrogen-incorporated $BaTiO_3$ thin films, we used x-ray absorption spectroscopy (XAS) assisted by theoretical simulations to investigate the detailed electronic structures of the films (Fig. 2, D and E, and figs. S15 and S16). We measured the XAS spectra at titanium $L_{2,3}$ edge with the polarization vector *E* of the incoming x-rays parallel (*E*//*c*) or perpendicular (*E*//*ab*) to the *c* axis of the films grown in different atmospheres (Fig. 2D). The overall line shape and peak energies of these three pairs of XAS spectra demonstrate that the titanium cations are predominantly in the 4+ charge state (rather than 3+; fig. S15B) with similar perovskite structure for all $BaTiO_3$ films (*29*). The spectra split into L_2 and L_3 regions because of strong spin-orbit interaction in the titanium 2*p* core hole states. Because of the crystal field, each L_2 and L_3 edge manifests itself in two peaks [i.e., e_g ($d_{x^2-y^2}$, $d_{3z^2-r^2}$) and t_{2g} (d_{xy}, d_{yz}, d_{xz})] (*30*). We found that the e_g peak at L_3 gradually gets broadened with increasing nitrogen content in the gas mixture, which is a sign of the hybridization-induced polar distortion of the TiO_6 octahedron (*31*–*33*). The degeneracy of the t_{2g} and e_g levels may be lifted by the tetragonal distortion (*30*), which can be evaluated by comparing the polarization dependence of titanium $L_{2,3}$ XAS spectra (*33*). X-ray linear dichroism (defined as the difference of XAS spectra measured between two orthogonal polarized x-rays), also increases with increasing nitrogen incorporation. For films grown in 100% oxygen, a very small energy shift of ~50 meV occurs at the L_3 e_g peak when the linearly polarized x-rays change from *E*//*ab* to *E*//*c*. In contrast, as the nitrogen content in the gas mixture increases to 100%, this energy shift at the L_3 e_g peak increases notably from 50 to ~320 meV. The L_3 e_g peak of the *E*//*c* spectrum arises from an electron transition to $d_{3z^2-r^2}$, while that of *E*//*ab* spectrum results from an electron transition to $d_{x^2-y^2}$. The energy shift from *E*//*c* to *E*//*ab* shows that the energy level of $d_{x^2-y^2}$ is higher than that of $d_{3z^2-r^2}$. As 320 meV is not a small value, this demonstrates a huge tetragonal distortion for films with nitrogen incorporation; consistent with the aforementioned XRD results. The energy shift of the L_3 t_{2g} peak is reversed (Fig. 2D), the *E*//*ab* spectrum has a lower energy than the *E*//*c* spectrum, meaning a lower energy level of d_{xy} than that of d_{yz}/d_{zx}. At first glance, this observation seems inconsistent with the XRD result of $c/a > 1$. However, this actually manifests that the Ti ion moves away from the TiO_6 octahedral center toward apical oxygens, as reported in previous studies (*30*, *34*).

We determine how large this Ti off-center displacement is by simulating the XAS spectra using a conventional theoretical approach, namely, the full multiplet CI cluster calculation (*35*, *36*). In the CI cluster calculation, we base the local solid-state effect on a TiX_6 cluster, where "*X*" represents the ligand anions that surround the titanium. We first simulate the XAS by keeping the titanium cation at the center of the TiX_6 octahedron and using $c/a \approx 1.11$, which corresponds to the XRD result of the film grown in 100% nitrogen. In this case, the Ti-*X* bond length along the *z* axis (*c* axis) is much longer than that in the *xy* plane (*ab* plane), which results in higher energies for the $d_{x^2-y^2}$ orbital in the e_g levels and the d_{xy} orbital in the t_{2g} levels, as shown as the 0 Å spectra in Fig. 2E. However, the simulated spectra are far from agreement with the experimental spectra. We then move the titanium cation along the *z* axis toward the apical ligand with a step size of 0.005 Å for the calculations (Fig. 2E shows only spectra with every 0.06 Å for simplicity). This brings up the energies of the $d_{3z^2-r^2}$ and d_{yz}/d_{zx} orbitals. The peak energy separation between the *E*//*ab* and *E*//*c* spectra decreases as the Ti ion displacement increases (Fig. 2E). The energy increase of the t_{2g} peak of *E*//*c* spectra is faster than that of the e_g peak. We found that with a Ti ion displacement of 0.42 Å the simulated spectra well reproduce the experimental spectra of the film grown in 100% nitrogen (Fig. 2E), and is well consistent with the aforementioned iDPC-STEM result (Fig. 2B). We applied the same calculation procedure for the spectra of the $BaTiO_3$ films prepared in 50% nitrogen and 100% oxygen (fig. S15, C and D) and summarized the results (Fig. 2F). The films grown in 100% nitrogen exhibit the largest titanium displacement along the out-of-plane direction compared to the films grown in 100% oxygen and 50% nitrogen (Fig. 2F), which is also much larger than the titanium displacement (~0.16 Å) in bulk $BaTiO_3$ (*37*). It is reasonable to conclude that the additional titanium off-center displacement of the $BaTiO_3$ film grown in 100% nitrogen is due to a stronger hybridization between titanium and nitrogen in comparison with that of titanium and oxygen.

Theoretical calculations

We corroborated the nitrogen substitution-induced polar distortion in $BaTiO_3$ thin film using first-principles calculations. In excellent agreement with the measured data, we found that isolated oxygen vacancies do not induce large polarization and *c*/*a* (table S1), while increasing the amount of nitrogen in the $BaTiO_3$ enhances the *c*/*a* ratio and polarization (table S1 and Fig. 3A). To rationalize this result further, we compare the charge-density distribution and density of states (DOS) between pure $BaTiO_3$ and N-doped $BaTiO_3$ with similar nitrogen composition as that in the films grown in 100% nitrogen (Fig. 3, B to D, and fig. S17). When an apical oxygen anion is replaced by nitrogen, the covalency between the anion and cations is found to be strongly enhanced (Fig. 3, C to D). In particular, it is found that the nearby titanium cations are shifted toward the nitrogen cations. The titanium-nitrogen hybridization is also substantially stronger than that of titanium-oxygen, as can be seen from the larger DOS from the nitrogen 2*p* orbitals below the Fermi level (Fig. 3D) as compared with the oxygen 2*p* orbitals in pure $BaTiO_3$ (Fig. 3B), which would give rise to the enhancement of Ti displacement and tetragonality with nitrogen substitution. Therefore, associating with larger polar distortion, the films grown in 100% nitrogen would induce stronger ferroelectricity than the films grown in 100% oxygen.

Ferroelectric properties

To further confirm the enhanced polar distortion, we measured the macroscopic ferroelectric properties of these films with ferroelectric polarization-electric field (*P*-*E*) hysteresis loops using symmetric SrRuO_3 capacitor structures. First, leakage current density studies

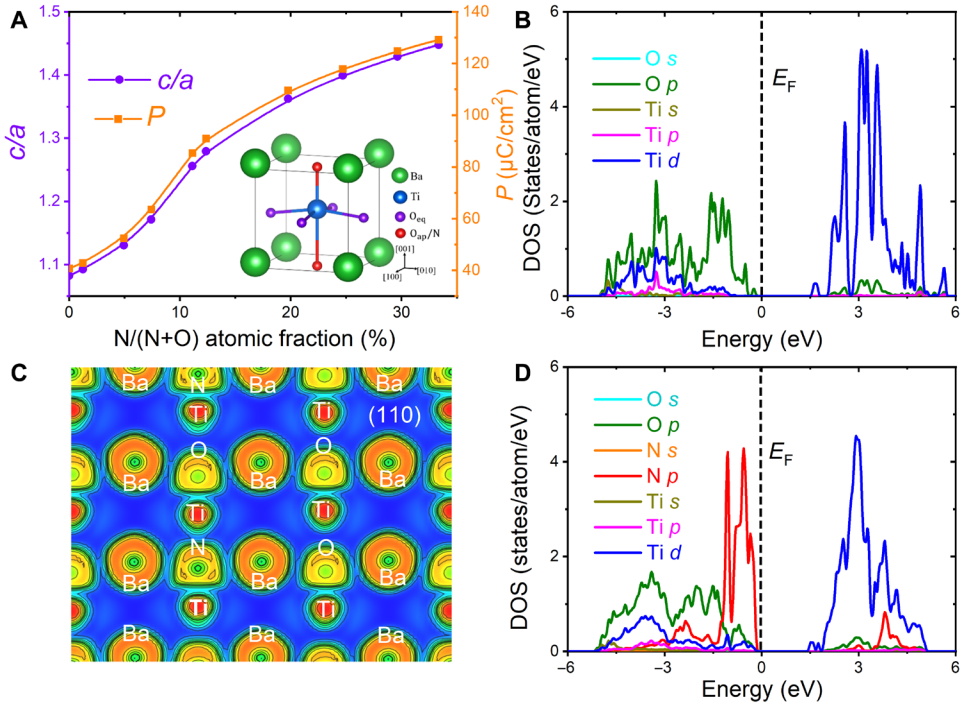

Fig. 3. Effect of N substitution from density functional theory calculations. (**A**) The calculated *c*/*a* ratio and polarization as a function of N atomic fraction at anionic sites. (**B**) The orbital-projected DOS for Ti and O in $BaTiO_3$. (**C**) Valence charge density on the (110) plane of the film with N atomic fraction of ~7 at %. (**D**) The orbital-projected DOS for Ti, O, and N in the film with N atomic fraction of ~7 at%. E_F is the Fermi energy of the films.

reveal symmetric and low-current characteristics (Fig. 4A). The films grown in 100% nitrogen have lower leakage current density as compared to the films grown in 100% oxygen and 50% nitrogen. The low leakage behavior is likely ascribed to the formation of defect dipoles (e.g., $V_O^{\bullet\bullet}$ and N_O') in the films. Such defect dipoles/complexes can serve as deep-level trap states, which work to reduce conductivity of the films (*24*). Characteristic ferroelectric hysteresis loops (Fig. 4B and fig. S18A) reveal distinct behaviors. One is the horizontal shift of the *P*-*E* hysteresis loops. As reported previously (*24*), defect dipoles can align in the direction of the polarization and act as local built-in fields that effectively pin the ferroelectric polarization, and thereby inducing the shifted *P*-*E* hysteresis loops. Besides, the different growth temperature of bottom and top $SrRuO_3$ electrodes may introduce an asymmetry between the top and bottom $SrRuO_3$-$BaTiO_3$ interfaces, and leading to an additional shift in the loops. In addition, the coercive filed of the films gradually increases with the increasing nitrogen content in gas mixture. This is attributed to the enhanced tetragonality and the possible defect pinning on polarization switching (*24*). The ferroelectric polarization also depends strongly on the nitrogen/oxygen gas mixture (namely, the polarization increases with nitrogen content; fig. S18B). The film grown in 100% oxygen exhibits "square" *P*-*E* hysteresis loop with low remnant (P_r ~ 20 μC/cm^2) and saturation (P_s ~ 25 μC/cm^2) polarization, in agreement with previous reports (*38*). As the percentage of nitrogen in the gas mixture increases to 100%, the films exhibit a typical well-saturated *P*-*E* hysteresis loop, but now with much higher P_r (~65 μC/cm^2) and P_s (~70 μC/cm^2). We further confirmed the robust ferroelectric behavior of the films grown in 100% nitrogen by measuring *P*-*E* hysteresis loops at different frequencies and fatigue cycles (fig. S19). To investigate whether the high ferroelectric polarization of the film grown in 100% nitrogen originates purely from the large *c*/*a* observed in these films, we used a large laser fluence to obtain film with similarly high *c*/*a* in the strained $BaTiO_3$ film but grown in 100% oxygen (fig. S20, A and B). Similar to previous studies (*39*), the ferroelectric polarization in these $BaTiO_3$ films with high *c*/*a* (~1.1) is only ~40 μC/cm^2 (fig. S20C); much smaller than the ferroelectric polarization in the films grown in 100% nitrogen. In addition, the results of XAS spectra also further demonstrate smaller titanium displacement in the films grown in 100% oxygen atmosphere with high laser fluence as compared to those grown in 100% nitrogen (fig. S21), since a uniform elongation of an octahedron does not enlarge much a polar distortion. Therefore, these results suggest that the polarization enhancement in the films grown in 100% nitrogen can be predominantly attributed to the incorporation of nitrogen into oxygen sublattice, which improves the hybridization between the titanium and the surrounding anions and thus drives a stronger polar distortion with larger titanium displacement (Figs. 2F and 3). Furthermore, additional factors, such as interstitial nitrogen incorporation and possible cation disorder, may also contribute to enhanced lattice distortion. Nonetheless, our findings underscore that a nitrogen-rich growth atmosphere serves as a fundamental factor in enhancing ferroelectric properties.

We also probed the robustness of this enhanced polarization in the films grown in 100% nitrogen to high temperatures (Fig. 4C). The temperature-dependent evolution of the *P*-*E* hysteresis loops reveals that the large ferroelectric polarization is robustly stable even at 400°C. Moreover, the large *c* lattice parameter can recover back when the film is cooled from 600°C to room temperature (fig. S22), further suggesting the excellent thermal stability of the film at high temperature. In turn, we determined the ferroelectric Curie temperature (T_C) of the films grown in different atmospheres by measuring the

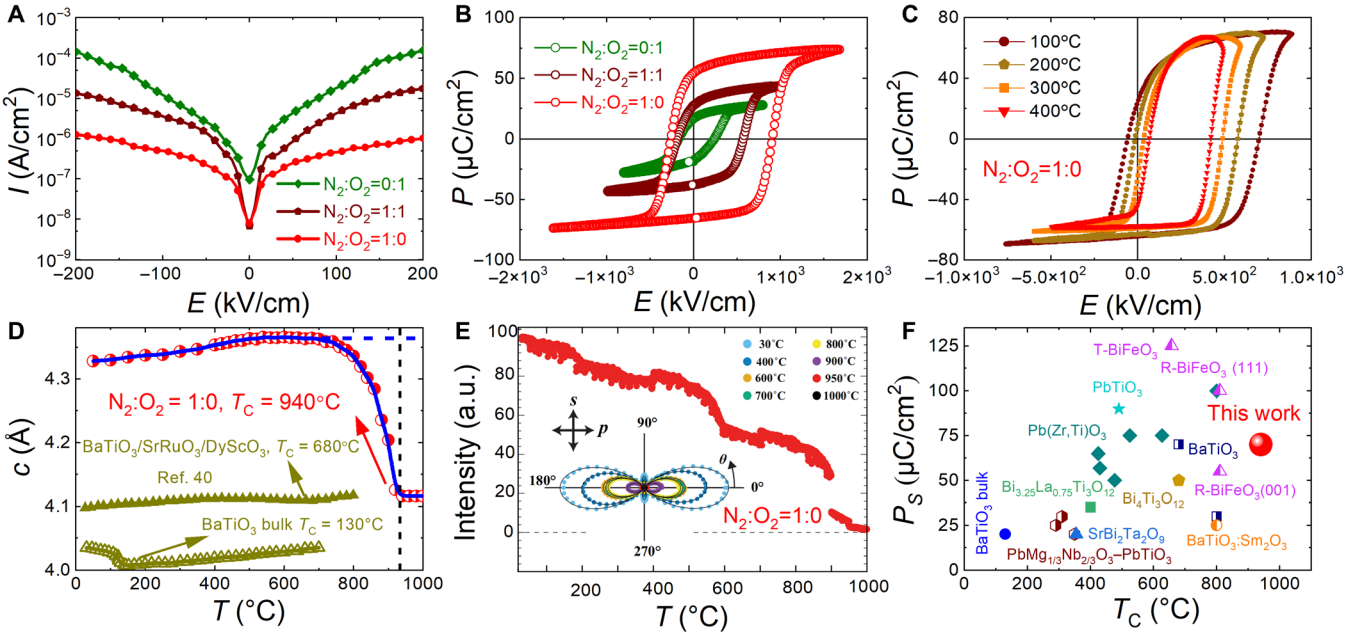

Fig. 4. Enhanced ferroelectric properties in $BaTiO_3$ film grown in nitrogen atmosphere. (**A**) Leakage current density as a function of DC electric field. (**B**) *P-E* loops of the films grown in different atmospheres at 10 kHz and room temperature. (**C**) *P-E* loops of the film grown in 100% nitrogen measured at different temperatures. (**D**) Temperature dependence of out-of-plane *c* lattice constant of the film grown in 100% nitrogen atmosphere. The temperature-dependent *c* lattice parameters of $BaTiO_3$ bulk and strained films are obtained from (*40*). (**E**) Temperature-dependent *p*-polarized SHG intensity (45° reflection geometry and *p*-polarized fundamental beam, i.e., $\theta = 0°$) of the film grown in 100% nitrogen. The discontinuity of SHG signal intensity with temperature is because the ramping was paused to collect polar plots at corresponding temperatures. The inset shows polar plots of *p*-polarized SHG intensity (radius) versus fundamental polarization, θ (azimuth) under different temperature. Circles and solid lines are experiment and theory, respectively. (**F**) Comparison of the polarization and Curie temperature of our films grown in 100% nitrogen with other representative ferroelectrics, including $BaTiO_3$ (*24*, *40*, *51*), $PbTiO_3$ (*52*), $Pb(Zr,Ti)O_3$ (*53*–*56*), $PbMg_{1/3}Nb_{2/3}O_3$-$PbTiO_3$ (*57*), $BiFeO_3$ (*34*, *58*, *59*), $SrBi_2Ta_2O_9$ (*60*), $BaTiO_3$:Sm_2O_3 (*61*), $Bi_4Ti_3O_{12}$ (*62*), and $Bi_{3.25}La_{0.75}Ti_3O_{12}$ (*63*).

temperature dependence of the *c* lattice parameter (Fig. 4D and fig. S23) and optical second-harmonic generation (SHG) (Fig. 4E and fig. S24). As we show, two regimes of thermal expansion over the temperature range from 25° to 1000°C separated by a kink that is characteristic of a structural phase transition is observed. The transition is typically attributed to the ferroelectric-paraelectric phase transition, which results in a pronounced negative thermal expansion phenomenon around Curie temperature (*24*, *40*). The high thermal stability is further supported by high-temperature annealing experiments, no impurities occur after annealing at temperature as high as 1000°C (figs. S25 to S27). Subsequently, the T_C of the films grown in 100% nitrogen is determined to be ~940°C, which is more than 800°C higher than that of bulk $BaTiO_3$ ($T_C = 130$°C). It is also ~300°C higher than that of strained $BaTiO_3$ films grown on rare-earth scandate substrates (*40*). We further performed SHG measurements to confirm the exceptional high Curie temperature of the film grown in 100% nitrogen atmosphere (Fig. 4E and fig. S24). Temperature-dependent SHG signal reveals that the film retains polar at least at 900°C, with a phase transition occurs at ~950°C, consistent with the temperature-dependent XRD results. Moreover, the enhanced ferroelectric polarization and Curie temperature are also demonstrated in other substrates, i.e., $DyScO_3(110)_o$ and $GdScO_3(110)_o$ (figs. S28 to S30). We further compare the spontaneous polarization and Curie temperature of the films with other ferroelectrics (Fig. 4F). The nitrogen-doped, lead-free $BaTiO_3$ films have higher Curie temperature than all other representative ferroelectrics. These results reveal an approach for manipulating the ferroelectric functionalities and enormous potential in high-temperature ferroelectric applications.

DISCUSSION

In summary, we demonstrate that nitrogen-incorporated $BaTiO_3$ thin films can be synthesized by pulsed-laser deposited technique in a nitrogen atmosphere. The nitrogen incorporation induces a unilateral strong hybridization between titanium and the surrounding anions, leading to a large titanium displacement (~0.4 Å) and correspondingly a large tetragonality (~1.11). As a result, the films show large enhancement in ferroelectric polarization to ~70 μC/cm^2 and T_C to ~1213 K; values which are ~2.8 and ~3 times larger than in bulk $BaTiO_3$, respectively. These results demonstrate that nitrogen incorporation is an effective avenue to enrich the perovskite structure and improve the ferroelectric properties of oxide thin films.

MATERIALS AND METHODS

Epitaxial thin-film synthesis

Heterostructures were fabricated by PLD (Arrayed Materials RP-B) technique using a KrF excimer laser (248 nm). To obtain steady state of target surface, $SrRuO_3$ and $BaTiO_3$ targets were sanded and sufficiently cleaned before film deposition. The $SrRuO_3$ bottom electrodes were grown in 100 mtorr of dynamic-oxygen pressure at 690°C from $SrRuO_3$ ceramic target at a laser fluence and laser repetition rate of 1.1 J/cm^2 and 5 Hz, respectively. The 30-nm-thick $BaTiO_3$ thin films were grown in 20 mtorr of dynamic mixed atmospheres with different ratios of N_2/O_2 (i.e., N_2:O_2 ratios of 0:1, 1:2, 1:1, 2:1, and 1:0), where the flow of N_2 and O_2 is controlled by flowmeter, while deposition temperature, laser repetition, and laser fluence are 620°C, 2 Hz, and 1.5 J/cm^2, respectively. To protect $BaTiO_3$ layer, top $SrRuO_3$

electrode layer has same deposition temperature (i.e., 620°C) with $BaTiO_3$ film, while other deposition parameters are same as $SrRuO_3$ bottom electrode. Besides, to compare with $BaTiO_3$ films grown in 100% N_2, a larger laser fluence of 1.9 J/cm^2 is used to obtain high *c*/*a* in $BaTiO_3$ films grown in 100% O_2 with 20 mtorr of gas pressure.

Structural analysis

The film morphology was determined by an Asylum Research MFP-3D-Infinity atomic force microscopy. The out-of-plane lattice parameters and RSM were measured using a high-resolution diffractometer with monochromated Cu $K\alpha_1$ source (Rigaku Smartlab 9 KW). XPS measurements were performed using an ESCALAB 250Xi instrument (Thermo Fisher Scientific) with the Al $K\alpha$ radiation ($h\nu = 1486.6$ eV) as the excitation source. In the XPS analysis, energy calibration was carried out by using C 1*s* peak at 284.6 eV. Besides, the element ratio is analyzed using the sensitivity factor method (*28*).

Cross-sectional TEM samples were prepared by slicing, gluing, grinding, dimpling, and ion milling using a Gatan precision ion polishing system. Samples were dimpled down to 8 μm before ion milling. In the ion milling process, the initial voltage was set to 5 kV and the angle was 9° via gradually reducing the voltage and angle to 3.5 kV and 4°, respectively. The final voltage was set to 0.3 kV to remove the amorphous layer produced by ion beam damage. In addition, some lamella specimens used for the TEM investigations were prepared by focus ion beam (FIB) system. Fischione NanoMill (mode 1040) operated at 500 eV was used to remove surface damage and contamination layers of the lamella specimens. An FEI Titan 80-200 ChemiSTEM microscope, equipped with annular detectors, a Super-X energy-dispersive x-ray spectrometer and a Gatan Enfinium ER (model 977) spectrometer, was used to characterize the atomic-scale structure information. The convergence semi-angle is 24.7 mrad and the collection semi-angle is 21.7 mrad at a dispersion of 0.25 eV/channel. iDPC images and EELS maps were recorded using aberration-corrected (scanning) transmission electron microscope [Titan Cubed 60 to 300 kV microscope (FEI) equipped with double Cs corrector from CEOS, and operated at 300 kV]. We adjusted the brightness and contrast of the entire iDPC images. The iDPC images were filtered.

Ferroelectric measurements

To suppress extrinsic metal-ferroelectric interface effects (i.e., imprint, asymmetric leakage, and lossy dielectric responses), the symmetric capacitor devices $SrRuO_3/BaTiO_3/SrRuO_3$ were prepared using wet chemical etchants and the detailed experimental progress can be obtained in (*41*). The electrode area was carefully calibrated to determine polarization value of the films. *P-E* hysteresis loop measurements were performed with a TF 3000 analyzer (aixACCT). The leakage behaviors of the thin films were analyzed using a Keithley 4200A-SCS semiconductor parameter analyzer. The temperature-dependent ferroelectric properties measurements were performed using a Semishare high-precision probe station (Semishare E4).

SHG measurements

SHG measurements were carried out with a pulsed fundamental beam generated by a regeneratively amplified Ti:sapphire system (wavelength of 800 nm and repetition rate of 1 kHz) in reflection geometry with the laser beam making the angle of 45° to the surface normal of the film. The polarization of the fundamental beam was rotated by an angle of θ by a half-wave plate, and the *p*-polarized and *s*-polarized SHG light was detected by a photomultiplier tube after passing through an analyzer. The temperature dependence of *p*-polarized SHG intensity (θ = 0°) was recorded on the heating process from 30° to 1000°C with Linkam stage. During the process, the ramping was paused and the temperature was stabilized at 400°, 600°, 700°, 800°, 900°, and 950°C to collect isothermal polar plots. Outlier values caused by an instant intensity fluctuation of the fundamental beam were excluded from the SHG intensity versus temperature plot. The theoretical expressions for the *p*-polarized and *s*-polarized SHG intensity ($I_p^{2\omega}$ and $I_s^{2\omega}$, respectively) are

$$I_p^{2\omega} \propto \left(f_{p1} f_{ps} d_{15} + \frac{f_{p1}^2 d_{31} + f_{p3}^2 d_{33}}{2} \right)^2 (\cos\theta)^4 + f_s^4 d_{31}^2 (\sin\theta)^4 + 2\left(f_{p1} f_{p3} d_{15} + \frac{f_{p1} d_{31} + f_{p3} d_{33}}{2} \right) f_s^2 d_{31} (\sin 2\theta)^2, \text{ and } I_s^{2\omega} \propto f_s^2 d_{15}^2 (\sin 2\theta)^2$$

where d_{ij} represents the SHG coefficients, and f_s, f_{p1}, and f_{p2} are the Fresnel coefficients.

Soft XAS

The XAS spectra were obtained at the TPS45A beamline of the National Synchrotron Radiation Research Center in Taiwan. A single crystal $SrTiO_3$ was simultaneously measured for energy calibration.

Full multiplet CI cluster calculation

In this theoretical approach, we build up the many-body quantum bases to take full advantage of the electron-electron multiplet effect and the spin-orbital coupling, which strongly influence the shape of the XAS lines. Parameters related to the electrons multiplet effect used in the calculations are: $F_2^{d-d} = 7.37$ eV, $F_4^{d-d} = 4.60$ eV, $F_2^{p-d} = 4.46$ eV, $G_1^{p-d} = 3.19$ eV, $G_3^{p-d} = 1.81$ eV. And the mono part of Coulomb repulsions are $U_{dd} = 5.0$ eV and $U_{pd} = 6.5$ eV. The parameters related to spin-orbital coupling are: $\xi_{d-d} = 0.016$ eV and $\xi_{p-d} = 3.927$ eV. For the local solid-states effect, we used the expansion of spherical harmonics to describe the crystal field potential around Ti ion and treated the surrounding oxygen and Ba ions as point charges:

$$V(r,\theta,\varphi) = \frac{4\pi}{2k+1} \sum_{k=0}^{l} \sum_{m=-k}^{k} A_{k,m} r^k Y_k^m(\varphi)$$

where $\langle r^2 \rangle = 0.28$ Å^2 and $\langle r^4 \rangle = 0.43$ Å^4 were used in the calculations. As for the O 2*p*–Ti 3*d* hybridization, we followed the prescription developed by Harrison (*42*). With this calculation we can evaluate the effect of the displacement of the Ti ion from its high symmetry point in the TiO_6 cluster on the XLD spectra.

First-principles calculations

First-principles calculations were performed within the density functional theory formalism using the projector augmented wave method as implemented in the Vienna Ab initio Simulation Package (*43*, *44*). The following valence electrons were treated explicitly: Ba $5s^2 5p^6 6s^2$, Ti $3s^2 3p^6 3d^2 4s^2$, O $2s^2 2p^4$, and N $2s^2 2p^3$. The generalized gradient approximation Perdew-Burke-Ernzerhof (PBE) exchange correlation functional was used in the modified form for solids (PBEsol) along with a plane wave cutoff energy of 500 eV (*45*, *46*). For the 5-atom perovskite unit cell, we used a 16 × 16 × 16 Monkhorst-Pack *k*-point mesh to optimize the structure until the

Hellmann-Feynman force on each atom was less than 0.0001 eV/Å. The optimized bulk $BaTiO_3$ lattice constants $a = 3.971$ Å and $c = 4.056$ Å are in good agreement with the previous computations (*47*, *48*). When simulating $BaTiO_3$ on $SrTiO_3$ substrate as in our experiment, an in-plane biaxial strain of −2.23% relative to the relaxed $BaTiO_3$ structure was applied. For defect structures, a $3 \times 3 \times 3$ supercell in terms of 5-atom pseudo-cubic perovskite cells was adopted, and $2 \times 2 \times 2$ Monkhorst-Pack *k*-point mesh was used. Relaxations were performed until the Hellmann-Feynman force was less than 0.01 eV/Å. The polarization was obtained via the Born effective charges. Calculations of the defect structures were based on the $3 \times 3 \times 3$ supercell (containing 135 atoms) under the strain conditions that correspond to $SrTiO_3$ substrate (−2.23%). As reported in other perovskite oxynitride epitaxial thin films (*7*, *8*), misfit strain can play a pivotal role in controlling the orientation of the Ti-N complex and determining the specific nitrogen locations within the oxygen octahedron. Furthermore, since nitrogen has a larger ionic radius than oxygen (*14*), the substrate-induced compressive strain would favor the location of nitrogen along out-of-plane direction and result in a specific, predominantly out-of-plane macroscopic lattice expansion (*7*, *49*). This preference corresponds to the preferential occupancy of nitrogen substitution at the apical site. Our calculation results further demonstrate that the apical substitution is numerically found to be energetically more favorable compared with the equatorial site, e.g., 446.1 meV/f.u. (or 2.4 meV/f.u.) lower by substituting one O with N in the unit cell (in the 135-atom supercell), consistent with previous studies (*7*, *8*, *49*). The charge density was calculated and visualized using VESTA software (*50*).

Supplementary Materials

This PDF file includes:

Supplementary Text
Figs. S1 to S30
Table S1
References

REFERENCES AND NOTES

1. F. Li, D. Lin, Z. Chen, Z. Cheng, J. Wang, C. C. Li, Z. Xu, Q. Huang, X. Liao, L.-Q. Chen, T. R. Shrout, S. Zhang, Ultrahigh piezoelectricity in ferroelectric ceramics by design. *Nat. Mater.* **17**, 349–354 (2018).
2. S. Ezhilvalavan, T.-Y. Tseng, Progress in the developments of (Ba,Sr)TiO_3 (BST) thin films for gigabit era DRAMs. *Mater. Chem. Phys.* **65**, 227–248 (2000).
3. S. Jin, T. H. Tiefel, M. McCormack, R. A. Fastnacht, R. Ramesh, L. H. Chen, Thousand fold change in resistivity in magnetoresistive La-Ca-Mn-O films. *Science* **264**, 413–415 (1994).
4. G. Kobayashi, Y. Hinuma, S. Matsuoka, A. Watanabe, M. Iqbal, M. Hirayama, M. Yonemura, T. Kamiyama, I. Tanaka, R. Kanno, Pure H^- conduction in oxyhydrides. *Science* **351**, 1314–1317 (2016).
5. K. Ogawa, H. Suzuki, C. Zhong, R. Sakamoto, O. Tomita, A. Saeki, H. Kageyama, R. Abe, Layered perovskite oxyiodide with narrow band gap and long lifetime carriers for water splitting photocatalysis. *J. Am. Chem. Soc.* **143**, 8446–8453 (2021).
6. P. J. Camp, A. Fuertes, J. P. Attfield, Subextensive entropies and open order in perovskite oxynitrides. *J. Am. Chem. Soc.* **134**, 6762–6766 (2012).
7. N. Vonruti, U. Aschauer, Anion order and spontaneous polarization in $LaTiO_2N$ oxynitride thin films. *Phys. Rev. Lett.* **120**, 046001 (2018).
8. D. Oka, Y. Hirose, H. Kamisaka, T. Fukumura, K. Sasa, S. Ishii, H. Matsuzaki, Y. Sato, Y. Ikuhara, T. Hasegawa, Possible ferroelectricity in perovskite oxynitride $SrTaO_2N$ epitaxial thin films. *Sci. Rep.* **4**, 4987 (2014).
9. R. Caracas, R. E. Cohen, Prediction of polar ordered oxynitride perovskites. *Appl. Phys. Lett.* **91**, 092902 (2007).
10. Y. Hirose, T. Hasegawa, Exploring metastable oxynitrides by thin film growth approach. *Bull. Chem. Soc. Jpn.* **94**, 1355–1363 (2021).
11. H. Kageyama, K. Hayashi, K. Maeda, J. P. Attfield, Z. Hiroi, J. M. Rondinelli, K. R. Poeppelmeier, Expanding frontiers in materials chemistry and physics with multiple anions. *Nat. Commun.* **9**, 772 (2018).
12. Y. Kobayashi, Y. Tsujimoto, H. Kageyama, Property engineering in perovskites via modification of anion chemistry. *Annu. Rev. Mat. Res.* **48**, 303–326 (2018).
13. T. Yamamoto, A. Chikamatsu, S. Kitagawa, N. Izumo, S. Yamashita, H. Takatsu, M. Ochi, T. Maruyama, M. Namba, W. Sun, T. Nakashima, F. Takeiri, K. Fujii, M. Yashima, Y. Sugisawa, M. Sano, Y. Hirose, D. Sekiba, C. M. Brown, T. Honda, K. Ikeda, T. Otomo, K. Kuroki, K. Ishida, T. Mori, K. Kimoto, T. Hasegawa, H. Kageyama, Strain-induced creation and switching of anion vacancy layers in perovskite oxynitrides. *Nat. Commun.* **11**, 5923 (2020).
14. R. D. Shannon, Revised effective ionic radii and systematic studies of interatomic distances in halides and chalcogenides. *Acta Crystallogr. A.* **32**, 751–767 (1976).
15. S. G. Ebbinghaus, H. P. Abicht, R. Dronskowski, T. Müller, A. Reller, A. Weidenkaff, Perovskite-related oxynitrides – Recent developments in synthesis, characterisation and investigations of physical properties. *Prog. Solid State Chem.* **37**, 173–205 (2009).
16. M. Jansen, H. P. Letschert, Inorganic yellow-red pigments without toxic metals. *Nature* **404**, 980–982 (2000).
17. T. Yajima, F. Takeiri, K. Aidzu, H. Akamatsu, K. Fujita, W. Yoshimune, M. Ohkura, S. Lei, V. Gopalan, K. Tanaka, C. M. Brown, M. A. Green, T. Yamamoto, Y. Kobayashi, H. Kageyama, A labile hydride strategy for the synthesis of heavily nitridized $BaTiO_3$. *Nat. Chem.* **7**, 1017–1023 (2015).
18. A. Shkabko, M. H. Aguirre, I. Marozau, T. Lippert, Y. H. Chou, R. E. Douthwaite, A. Weidenkaff, Synthesis and transport properties of $SrTiO_{3-x}N_y/SrTiO_{3-\delta}$ layered structures produced by microwave-induced plasma nitridation. *J. Phys. D Appl. Phys.* **42**, 145202 (2009).
19. S. Aggarwal, S. R. Perusse, C. W. Tipton, R. Ramesh, H. D. Drew, T. Venkatesan, D. B. Romero, V. B. Podobedov, A. Weber, Effect of hydrogen on Pb(Zr,Ti)O_3-based ferroelectric capacitors. *Appl. Phys. Lett.* **73**, 1973–1975 (1998).
20. D. H. Lowndes, D. B. Geohegan, A. A. Puretzky, D. P. Norton, C. M. Rouleau, Synthesis of novel thin-film materials by pulsed laser deposition. *Science* **273**, 898–903 (1996).
21. I. Marozau, A. Shkabko, G. Dinescu, M. Döbeli, T. Lippert, D. Logvinovich, M. Mallepell, C. W. Schneider, A. Weidenkaff, A. Wokaun, Pulsed laser deposition and characterization of nitrogen-substituted $SrTiO_3$ thin films. *Appl. Surf. Sci.* **255**, 5252–5255 (2009).
22. I. Marozau, A. Shkabko, M. Döbeli, T. Lippert, D. Logvinovich, M. Mallepell, C. W. Schneider, A. Weidenkaff, A. Wokaun, Optical properties of nitrogen-substituted strontium titanate thin films prepared by pulsed laser deposition. *Materials* **2**, 1388–1401 (2009).
23. M. Tyunina, S. Cichon, N. Nepomniashchaia, T. Kocourek, P. Svora, M. Savinov, V. Vetokhina, M. Klementova, A. Dejneka, In-situ nitrided pulsed-laser-deposited $SrTiO_3$ films. *Next Materials* **1**, 100003 (2023).
24. A. R. Damodaran, E. Breckenfeld, Z. H. Chen, S. Lee, L. W. Martin, Enhancement of ferroelectric Curie temperature in $BaTiO_3$ films via strain-induced defect dipole alignment. *Adv. Mater.* **26**, 6341–6347 (2014).
25. I. Lazic, E. G. T. Bosch, S. Lazar, Phase contrast STEM for thin samples: Integrated differential phase contrast. *Ultramicroscopy* **160**, 265–280 (2016).
26. C. Di Valentin, E. Finazzi, G. Pacchioni, A. Selloni, S. Livraghi, M. C. Paganini, E. Giamello, N-doped TiO_2: Theory and experiment. *Chem. Phys.* **339**, 44–56 (2007).
27. R. Asahi, T. Morikawa, T. Ohwaki, K. Aoki, Y. Taga, Visible light photocatalysis in nitrogen-doped titanium oxides. *Science* **293**, 269–271 (2001).
28. C. D. Wagner, L. E. Davis, M. V. Zeller, J. A. Taylor, R. H. Raymond, L. H. Gale, Empirical atomic sensitivity factors for quantitative analysis by electron spectroscopy for chemical analysis. *Surf. Interface Anal.* **3**, 211–225 (1981).
29. J. S. Lee, Y. W. Xie, H. K. Sato, C. Bell, Y. Hikita, H. Y. Hwang, C. C. Kao, Titanium dxy ferromagnetism at the $LaAlO_3/SrTiO_3$ interface. *Nat. Mater.* **12**, 703–706 (2013).
30. Y. Song, X. Liu, F. Wen, M. Kareev, R. Zhang, Y. Pei, J. Bi, P. Shafer, A. T. N'Diaye, E. Arenholz, S. Y. Park, Y. W. Cao, J. Chakhalian, Unconventional crystal-field splitting in noncentrosymmetric $BaTiO_3$ thin films. *Phys. Rev. Mater.* **4**, 024413 (2020).
31. J. C. Jan, K. P. K. Kumar, J. W. Chiou, H. M. Tsai, H. L. Shih, H. C. Hsueh, S. C. Ray, K. Asokan, W. F. Pong, M. H. Tsai, S. Y. Kuo, W. F. Hsieh, Effect of the Ca content on the electronic structure. *Appl. Phys. Lett.* **83**, 3311–3313 (2003).
32. E. Eberg, A. T. J. van Helvoort, R. Takahashi, M. Gass, B. Mendis, A. Bleloch, R. Holmestad, T. Tybell, Electron energy loss spectroscopy investigation of Pb and Ti hybridization with O at the $PbTiO_3/SrTiO_3$ interface. *J. Appl. Phys.* **109**, 034104 (2011).
33. C. Schmitz-Antoniak, D. Schmitz, P. Borisov, F. M. de Groot, S. Stienen, A. Warland, B. Krumme, R. Feyerherm, E. Dudzik, W. Kleemann, H. Wende, Electric in-plane polarization in multiferroic $CoFe_2O_4/BaTiO_3$ nanocomposite tuned by magnetic fields. *Nat. Commun.* **4**, 2051 (2013).
34. J. X. Zhang, Q. He, M. Trassin, W. Luo, D. Yi, M. D. Rossell, P. Yu, L. You, C. H. Wang, C. Y. Kuo, J. T. Heron, Z. Hu, R. J. Zeches, H. J. Lin, A. Tanaka, C. T. Chen, L. H. Tjeng, Y. H. Chu, R. Ramesh, Microscopic origin of the giant ferroelectric polarization in tetragonal-like $BiFeO_3$. *Phys. Rev. Lett.* **107**, 147602 (2011).
35. A. Tanaka, J. Takeo, Resonant 3*d*, 3*p* and 3*s* photoemission in transition metal oxides predicted at 2*p* threshold. *J. Phys. Soc. Jpn.* **63**, 2788–2807 (1994).

36. F. M. F. De Groot, X-ray absorption and dichroism of transition metals and their compounds. *J. Electron. Spectrosc. Relat. Phenom.* **67**, 529–622 (1994).
37. G. H. Kwei, A. C. Lawson, S. J. L. Billinge, S. W. Cheong, Structures of the ferroelectric phases of barium titanate. *J. Phys. Chem.* **27**, 2368–2377 (1993).
38. W. Peng, J. A. Zorn, J. Mun, M. Sheeraz, C. J. Roh, J. Pan, B. Wang, K. Guo, C. W. Ahn, Y. P. Zhang, K. Yao, J. S. Lee, J. S. Chung, T. H. Kim, L. Q. Chen, M. Kim, L. F. Wang, T. W. Noh, Constructing polymorphic nanodomains in $BaTiO_3$ films via epitaxial symmetry engineering. *Adv. Funct. Mater.* **30**, 1910569 (2020).
39. N. Yanase, K. Abe, N. Fukushima, T. Kawakubo, Thickness dependence of ferroelectricity in heteroepitaxial $BaTiO_3$ thin film capacitors. *Jpn. J. Appl. Phys.* **38**, 5305–5308 (1999).
40. K. J. Choi, M. Biegalski, Y. L. Li, A. Sharan, J. Schubert, R. Uecker, P. Reiche, Y. B. Chen, X. Q. Pan, V. Gopalan, L. Q. Chen, D. G. Schlom, C. B. Eom, Enhancement of ferroelectricity in strained $BaTiO_3$ thin films. *Science* **306**, 1005–1009 (2004).
41. D. Weber, R. Vofély, Y. H. Chen, Y. Mourzina, U. Poppe, Variable resistor made by repeated steps of epitaxial deposition and lithographic structuring of oxide layers by using wet chemical etchants. *Thin Solid Films* **533**, 43–47 (2013).
42. W. A. Harrison, *Electronic Structure and the Properties of Solids: The Physics of the Chemical Bond* (Courier Corporation, 2012).
43. G. Kresse, D. Joubert, From ultrasoft pseudopotentials to the projector augmented-wave method. *Phys. Rev. B.* **59**, 1758–1775 (1999).
44. G. Kresse, J. Furthmuller, Efficient iterative schemes for ab initio total-energy calculations using a plane-wave basis set. *Phys. Rev. B. Condens. Matter* **54**, 11169–11186 (1996).
45. J. P. Perdew, K. Burke, M. Ernzerhof, Generalized gradient approximation made simple. *Phys. Rev. Lett.* **77**, 3865–3868 (1996).
46. J. P. Perdew, A. Ruzsinszky, G. I. Csonka, O. A. Vydrov, G. E. Scuseria, L. A. Constantin, X. Zhou, K. Burke, Restoring the density-gradient expansion for exchange in solids and surfaces. *Phys. Rev. Lett.* **100**, 136406 (2008).
47. G. Shirane, H. Danner, R. Pepinsky, Neutron diffraction study of orthorhombic $BaTiO_3$. *Phys. Rev.* **105**, 856–860 (1957).
48. D. I. Bilc, R. Orlando, R. Shaltaf, G. M. Rignanese, J. Íñiguez, P. Ghosez, Hybrid exchange-correlation functional for accurate prediction of the electronic and structural properties of ferroelectric oxides. *Phys. Rev. B.* **77**, 165107 (2008).
49. Y. I. Kim, W. Si, P. M. Woodward, E. Sutter, S. Park, T. Vogt, Epitaxial thin-film deposition and dielectric properties of the perovskite oxynitride $BaTaO_2N$. *Chem. Mater.* **19**, 618–623 (2007).
50. K. Momma, F. Izumi, VESTA: A three-dimensional visualization system for electronic and structural analysis. *J. Appl. Cryst.* **41**, 653–658 (2008).
51. W. Pan, Q. Zhang, A. S. Bhalla, L. E. Cross, Field-induced strain in single-crystal $BaTiO_3$. *J. Am. Ceram. Soc.* **71**, C-302–C-305 (1988).
52. S. Saremi, R. Xu, L. R. Dedon, J. A. Mundy, S. L. Hsu, Z. Chen, A. R. Damodaran, S. P. Chapman, J. T. Evans, L. W. Martin, Enhanced electrical resistivity and properties via ion bombardment of ferroelectric thin films. *Adv. Mater.* **28**, 10750–10756 (2016).
53. S. Pandya, G. A. Velarde, R. Gao, A. S. Everhardt, J. D. Wilbur, R. Xu, J. T. Maher, J. C. Agar, C. Dames, L. W. Martin, Understanding the role of ferroelastic domains on the pyroelectric and electrocaloric effects in ferroelectric thin films. *Adv. Mater.* **31**, e1803312 (2019).
54. Y. Ehara, S. Utsugi, M. Nakajima, T. Yamada, T. Iijima, H. Taniguchi, M. Itoh, H. Funakubo, Spontaneous polarization estimation from the soft mode in strain-free epitaxial polar axis-oriented $Pb(Zr,Ti)O_3$ thick films with tetragonal symmetry. *Appl. Phys. Lett.* **98**, 141914 (2011).
55. B. Noheda, D. E. Cox, G. Shirane, J. A. Gonzalo, L. E. Cross, S. E. Park, A monoclinic ferroelectric phase in the $Pb(Zr_{1-x}Ti_x)O_3$ solid solution. *Appl. Phys. Lett.* **74**, 2059–2061 (1999).
56. C. Huang, Z. Liao, M. Li, C. Guan, F. Jin, M. Ye, X. Zeng, T. Zhang, Z. Chen, Y. Qi, P. Gao, L. Chen, A highly strained phase in $PbZr_{0.2}Ti_{0.8}O_3$ films with enhanced ferroelectric properties. *Adv. Sci.* **8**, 2003582 (2021).
57. J. Kim, H. Takenaka, Y. B. Qi, A. R. Damodaran, A. Fernandez, R. Gao, M. R. McCarter, S. Saremi, L. Chung, A. M. Rappe, L. W. Martin, Epitaxial strain control of relaxor ferroelectric phase evolution. *Adv. Mater.* **31**, e1901060 (2019).
58. J. Wang, J. B. Neaton, H. Zheng, V. Nagarajan, S. B. Ogale, B. Liu, D. Viehland, V. Vaithyanathan, D. G. Schlom, U. V. Waghmare, N. A. Spaldin, K. M. Rabe, M. Wuttig, R. Ramesh, Epitaxial $BiFeO_3$ multiferroic thin film heterostructures. *Science* **299**, 1719–1722 (2003).
59. M. Lachheb, Q. Zhu, S. Fusil, Q. Wu, C. Carrétéro, A. Vecchiola, M. Bibes, D. Martinotti, C. Mathieu, C. Lubin, A. Pancotti, X. Li-Bourrelier, A. Gloter, B. Dkhil, V. Garcia, N. Barrett, Surface and bulk ferroelectric phase transition in super-tetragonal $BiFeO_3$ thin films. *Phys. Rev. Mater.* **5**, 024410 (2021).
60. K. Amanuma, T. Hase, Y. Miyasaka, Preparation and ferroelectric properties of $SrBi_2Ta_2O_9$ thin films. *Appl. Phys. Lett.* **66**, 221–223 (1995).
61. S. A. Harrington, J. Zhai, S. Denev, V. Gopalan, H. Wang, Z. Bi, S. A. Redfern, S. H. Baek, C. W. Bark, C. B. Eom, Q. Jia, M. E. Vickers, J. L. Macmanus-Driscoll, Thick lead-free ferroelectric films with high Curie temperatures through nanocomposite-induced strain. *Nat. Nanotechnol.* **6**, 491–495 (2011).
62. S. E. Cummins, L. E. Cross, Electrical and optical properties of ferroelectric $Bi_4Ti_3O_{12}$ single crystals. *J. Appl. Phys.* **39**, 2268–2274 (1968).
63. H. N. Lee, D. Hesse, N. Zakharov, U. Gosele, Ferroelectric $Bi_{3.25}La_{0.75}Ti_3O_{12}$ films of uniforma-axis orientation on silicon substrates. *Science* **296**, 2006–2009 (2002).
64. A. Kumar, J. N. Baker, P. C. Bowes, M. J. Cabral, S. Zhang, E. C. Dickey, D. L. Irving, J. M. LeBeau, Atomic-resolution electron microscopy of nanoscale local structure in lead-based relaxor ferroelectrics. *Nat. Mater.* **20**, 62–67 (2021).
65. S. Cai, Y. Lun, D. Ji, P. Lv, L. Han, C. Guo, Y. Zang, S. Gao, Y. Wei, M. Gu, C. Zhang, Z. Gu, X. Wang, C. Addiego, D. Fang, Y. Nie, J. Hong, P. Wang, X. Pan, Enhanced polarization and abnormal flexural deformation in bent freestanding perovskite oxides. *Nat. Commun.* **13**, 5116 (2022).
66. G. Panchal, D. K. Shukla, R. J. Choudhary, V. R. Reddy, D. M. Phase, The effect of oxygen stoichiometry at the interface of epitaxial $BaTiO_3/La_{0.7}Sr_{0.3}MnO_3$ bilayers on its electronic and magnetic properties. *J. Appl. Phys.* **122**, 085310 (2017).
67. N. Strkalj, G. De Luca, M. Campanini, S. Pal, J. Schaab, C. Gattinoni, N. A. Spaldin, M. D. Rossell, M. Fiebig, M. Trassin, Depolarizing-field effects in epitaxial capacitor heterostructures. *Phys. Rev. Lett.* **123**, 147601 (2019).
68. S. M. Selbach, M. A. Einarsrud, T. Grande, On the thermodynamic stability of $BiFeO_3$. *Chem. Mater.* **21**, 169–173 (2009).
69. L. Zhang, J. Chen, L. Fan, O. Diéguez, J. Cao, Z. Pan, Y. Wang, J. Wang, M. Kim, S. Deng, J. Wang, H. Wang, J. Deng, R. Yu, J. Scott, X. Xing, Giant polarization in super-tetragonal thin films through interphase strain. *Science* **361**, 494–497 (2018).

Acknowledgments

Funding: This work was supported by National Natural Science Foundation of China (grant nos. 92477129 and 52372105) and Shenzhen Science and Technology Program (grant no. KQTD20200820113045083). Z.C. has been supported by State Key Laboratory of Precision Welding & Joining of Materials and Structures (grant no. 24-Z-13), "the Fundamental Research Funds for the Central Universities" (grant no. 2024FRFK03012) and "Talent Recruitment Project of Guangdong" (grant no. 2019QN01C202). Y.C.-K. acknowledges the financial support from the Ministry of Science and Technology in Taiwan under grant no. MOST 110-2112-M-A49-002-MY3 (Research Project for Newly-recruited Personnel). Y.C.-K. and C.-F.C. acknowledge support from the Max Planck-POSTECH-Hsinchu Center for Complex Phase Materials. L.B. thanks the ONR grant no. N00014-21-1-2086 and the Vannevar Bush Faculty Fellowship (VBFF) grant no. N00014-20-1-2834 from the Department of Defense. L.W.M. acknowledges support from the National Science Foundation under grant DMR-2102895. S.D. acknowledges Science and Engineering Research Board (SRG/2022/000058) and Indian Institute of Science start up grant for financial support. X.-K.W. was supported by grants of the National High-Level Youth Talents Program (grant no. 0040/X2450224), the Science and Technology Projects of Innovation Laboratory for Sciences and Technologies of Energy Materials of Fujian Province (IKKEM) (grant no. 0040/K5023001), and the Xiamen University President's Fund Program (grant no. 0040/ZK1227). L.C. acknowledges the supports by the National Natural Science Foundation of China (grant no. 51972160), the National Key R&D Program of China (no. 2022YFA1402903), the Guangdong Provincial Key Laboratory Program (grant no. 2021B1212040001), and SUSTech Core Research Facilities. B.X. and Xu.M. acknowledge financial support from National Natural Science Foundation of China (grant no. 12074277), Projects of International Cooperation and Exchanges NSFC (grant no. 12311530693), Jiangsu Shuangchuang Project (JSSCTD202209), and the support from Priority Academic ProgramDevelopment (PAPD) of Jiangsu Higher Education Institutions. S.Y. and V.G. acknowledge support from the National Science Foundation grant no. DMR-2210933 for optical SHG characterization. S.H. and V.G. acknowledge support from the Department of Energy grant number DE-SC0012375 for optical SHG characterization. **Author contributions:** Z.H.C. conceived and supervised this study; T.W., S.P., and S.W. fabricated the films, performed the XRD, and ferroelectric measurements; Xu.M. and B.X. performed first-principles calculations; F.G., X.-K.W., Y.T., Y.-L.Z., and Xi.M. performed the STEM characterizations; C.K., Y.-C.K., and C.-F.C. conducted the XAS measurements; S.Y., S.H., and V.G. conducted the SHG measurements; Z.Y. and K.H.L.Z. performed the XPS experiments; T.W., Xu.M., and Z.H.C. wrote the original draft; Z.H.C., T.W., C.K., S.Y., S.H., V.G., X.-K.W., S.D., Y.T., C.-F.C., B.X., L.B., and L.W.M. discussed the data and edited the manuscript. All authors commented on the manuscript. **Conflict of interest:** The authors declare that they have no competing interests. **Data and materials availability:** All data needed to evaluate the conclusions in the paper are present in the paper and/or the Supplementary Materials.

Submitted 2 September 2024
Accepted 5 December 2024
Published 10 January 2025
10.1126/sciadv.ads8830